Version: 1.0
Author(s): D.K. Cho, S.Y. Choi, L. Feligioni, M. Narain

Send comments to d0-run2eb-004@fnal.gov
by July 2, 2006.

DØ- CONF note 5154

Search for Techniparticles at DØ

To be presented at the 2006 summer conferences

The DØ Collaboration
URL: http://www-d0.fnal.gov

(Dated: July 1, 2006)

We search for the Technicolor process $\rho_T/\omega \to \pi_T W$ using events with one electron and two jets in 388 pb^{-1} of integrated luminosity recorded by the DØ experiment at Fermilab. As predicted by the Technicolor Straw Man Model [1], π_Ts decay dominantly into $b\bar{b}$, $b\bar{c}$, or $\bar{b}c$, depending on their charge. We select events containing b and c-quarks by identifying their secondary decay vertices within jets. We use two analysis methods, based on topological variables, one is cut-based and the other used neural networks for separation of signal and backgrounds. In the absence of an observed excess above the standard model prediction for expected backgrounds we define an excluded region, as a function of ρ_T and π_T masses and a given set of model parameters.

Introduction

Technicolor (TC), first formulated by Weinberg and Susskind [2, 3], is a non-Abelian gauge theory modeled after quantum chromo dynamics (QCD). TC provides a dynamical explanation of electroweak symmetry breaking (ESB) by predicting a new strong $SU(N_{TC})$ gauge theory and new fermions, "techniquarks". Just as in QCD, in the low-energy limit of TC a spontaneous breaking of the chiral symmetry leads to breaking the electroweak interactions down to electromagnetism. The Nambu-Goldstone bosons produced in this process are called technipions π_T, in analogy with the pions of QCD. Three of these technipions become the longitudinal components of the W and Z bosons which acquire mass in the process.

An additional gauge field, Extended Technicolor (ETC) [4, 5], couples Standard Model fermions and technifermions, producing a mechanism for generating quark and lepton masses. By imposing a particular dependence of TC coupling constants, Walking Technicolor (WTC) [6] makes it possible to avoid the dangerous increase of the ordinary fermion coupling responsible for flavor-changing neutral currents. Still, to arrive at masses as high as the top quark mass, another interaction, Topcolor, is necessary, giving rise to Topcolor-assisted Technicolor models (TC2) [7].

All the extensions of the basic Technicolor model require a large number N_D of technifermion doublets. In general, the Technicolor scale Λ_{TC} depends on the number of technifermion doublets $\Lambda_{TC} \approx F_{TC}/\sqrt{N_D}$, where F_{TC} is the technipion decay constant. For large N_D the lowest lying technihadrons have masses on the order of few hundred GeV. This scenario is usually referred to as Low-Scale Technicolor.

Low Scale TC models predict the existence of scalar mesons, the technipions ($\pi_T^{\pm}$ and π_T^0), and vector mesons (ρ_T and ω_T). These technihadron states are expected to be produced with substantial rates at the Tevatron. Vector Technimesons decay to gauge boson (γ, W, Z) plus technipions or fermion-antifermion pairs. The production cross sections and branching fractions depend on:

- the masses of ρ_T (M_{ρ_T}) and ω_T (M_{ω_T});
- the technicolor-charges of the technifermions;
- the mass differences between the vector mesons and technipions which determine the spectrum of accessible decay channels;
- two mass parameters, M_A for axial-vector and M_V for vector couplings.

The parameter M_V controls the rate for $\omega_T \to \gamma + \pi_T^0$. and is unknown *a priori*. Scaling from the QCD decay $\omega \to \gamma + \pi^0$ the authors of Ref. [1] suggest a value of several 100 GeV. We set $M_A = M_V = 500$ GeV. For all other parameters, we use the default values quoted in Table III of Ref. [1]. Also, the strength of technipions coupling to the SM particles depends on the mass of SM particle, therefore π_T's in the mass range considered will decay most of the time into $b\bar{b}$, $b\bar{c}$, or $\bar{b}c$, depending on their charge.

In the last few years a new version of the TCSM [1], renamed as TCSM2, has been implemented in Monte Carlo event generator PYTHIA 6.2 [1]. Changes have been made to the modeling of the $SU(3)_C$ single sector that affect mainly results for e^+e^- colliders. In the TC model used in the earlier searches by D0 and CDF, no decay for technivector mesons into transversely polarized gauge bosons were considered [9]. The effect on the predictions for the Tevatron is to lower the cross sections for some of the modes. These can be a factor of two below the ones predicted by TCSM. Hence, the results from the analysis presented in this note cannot be directly compared to the previous published results from the Tevatron. As for comparing with the results from LEP experiments, according to Ken Lane, the author of TCSM2 models, there were couple of assumptions made which are inappropriate, e.g. the limits were computed by looking for $e^+e^- \to W^+W^-$, but the TC programs for those are not good for LEP as they used a narrow resonance approximation for technirho production. Also, interference between TC and SM amplitudes which give rise to the longitudinal and transverse W are not taken into account correctly for the LEP results.

Data Event Selection and Modeling of Signal and Background Events

In the DØ detector, described in [10], $W\pi_T$ production is identified by the presence of one isolated electron and missing transverse momentum ($\not{p}_T$) from the undetected neutrino from the decay of the W boson, and two jets of hadrons coming from the fragmentation of the quarks from the decay of the technipion. We search for events with this signature in the data collected by DØ from April 2002 until July 2004. After requiring that at least one single electron trigger fired and good quality data, we are left with an integrated luminosity of 388 pb^{-1}.

We select events in which there is exactly one well-identified electron based on tracking and calorimeter data with transverse momentum $p_T > 20$ GeV and pseudorapidity $|\eta| < 1.1$. To reject events with $Z \to ee$ decays, we require that there must not be any other electron candidates, with neither tracking nor pseudorapidity requirements, in the

Process	Generator	Cross Section (in pb)	Number of Events
$t\bar{t} \to \ell\nu\ b\bar{b}\ q\bar{q}$	pythia	2.95	26000
$t\bar{t} \to \ell^+\nu\ell^-\nu\ b\bar{b}$	pythia	0.695	46750
$W^* \to tb \to (e\nu + \tau\nu)bb$	pythia	0.115	32500
$qtb \to q\ (e\nu + \tau\nu)bb$	pythia	0.258	33000
$W(\to e\nu) + b\bar{b}$	alpgen	3.35	99500
$W + heavy\ flavors$	alpgen	287.3	189500
$W(\to e + \nu)$	pythia	2684	300000
$W(\to \tau + \nu)$	pythia	2684	200000
$WZ \to \ell + \nu\ b\bar{b}$	pythia	0.0542	49000
$Z \to e^+e^-(m_{\ell\ell} = 15 - 60)$	pythia	528	19500
$Z \to e^+e^-(m_{\ell\ell} = 60 - 130)$	pythia	245.7	247000
$Z(\to e^+e^-) + b\bar{b}$	pythia	0.539	98000

TABLE I: Physics Background Processes. We list their cross sections, the uncertainty on the cross section, and number of events generated and processed through GEANT.

detector. We further require the presence of two jets with $p_T > 20$ GeV and $|\eta| < 2.5$. We veto on the presence of any other jets in order to reduce the contamination from standard model processes with high jet multiplicity, such as $t\bar{t}$ or W+jets production. Two different definitions are used to estimate the transverse momentum of the neutrino. The object based $\not{p}_T^{obj}$ is defined as the negative vectorial sum of the jet and electron momenta. The calorimeter based $\not{p}_T$, also takes in consideration energy depositions not assigned to the electron and the jets. We accept all events with $\not{p}_T > 20$ GeV, $\not{p}_T^{obj} > 20$ GeV and transverse mass $m_T > 30$ GeV calculated from electron p_T and $\not{p}_T^{obj}$, the latter being the preferred missing energy algorithm since it is reproducible with fast monte carlo techniques.

After the kinematic selection using jets, electron, and missing momentum, we are left with 4664 events.

To further reduce backgrounds, we use the long lifetime of b-flavored hadrons. Tracks from decay products of b-hadrons may not project back to the proton-antiproton collision, but have a significant impact parameter. They can therefore be identified and used to reconstruct the decay vertex of the b-hadron. A jet is tagged as a b-jet if there is a secondary decay vertex within $\Delta R = \sqrt{(\Delta\eta)^2 + (\Delta\phi)^2} < 0.5$ of the jet axis [11].

Our final Wjb data set of 117 events is defined by all selected events with at least one b-tagged jet.

We simulate the following standard model processes that contribute to the Wjb data set using different Monte Carlo generators and GEANT [12]. These physics processes are listed with their cross sections in Table I.

- top-quark production: $t\bar{t}$ events have higher jet multiplicity than $W\pi_T$ decays. They only produce the same signature, if one top quark decays to $e\nu b$ and some of the decay products of the other top quark are undetected. Single top-quark production is more likely to give rise to events that pass our final selection but it has a smaller cross section. Events with top quarks are generated using PYTHIA [13].

- $W(\to e\nu)$ + heavy flavor production: Events in which a W boson is produced together with two or more jets, at least one from the fragmentation of a heavy quark, are an irreducible source of background to this analysis. Among these processes are: W boson produced together with two b-jets ($Wb\bar{b}$), W plus one b-jet, and W plus at least one c-jet. $W + b\bar{b}$ production is generated and analyzed separately, all the others are referred to as W+heavy flavors. These processes are generated using ALPGEN [14].

- $Z(\to ee)$ + heavy flavor production.

- $W(\to e\nu) + Z(\to b\bar{b}$ or $c\bar{c})$ production.

When estimating the expected number of events from each of these backgrounds, each Monte Carlo event is weighted by the probability that at least one of its jets is tagged with a secondary vertex. The tagging probability is parameterized as a function of jet flavor, p_T, and η. The efficiency of tagging a jet from the fragmentation of a b-quark is derived from jet data that are enriched in b-quark contents by the requirement that there is a muon in the event. Using secondary vertex tagging together with muon tagging of semileptonic b-decays allows us to set up a system of linear equations that can be solved for the tagging probability of b-jets. The probability of tagging a c-jet is derived from the tagging probability for b-jets by multiplying by the ratio of tagging probabilities for c and b-jets, derived from Monte Carlo. The probability to tag a light-quark or gluon jet we derive from a set of dijet events, corrected for the contamination by c and b-jets.

The Monte Carlo events are also weighted by the ratio of jet and electron finding efficiencies in Monte Carlo and collider data. The latter is measured in $Z \to ee$ events in both data and Monte Carlo. The scale factor is 0.913±0.015.

Process	Number of Events
DATA:	117
Physics Backgrounds:	
$t\bar{t} \to \ell\nu\ b\bar{b}\ q\bar{q}$	7.9
$t\bar{t} \to \ell^+\nu\ell^-\nu\ b\bar{b}$	14.1
$W^* \to tb \to (e\nu + \tau\nu)bb$	3.5
$qtb \to q\ (e\nu + \tau\nu)bb$	4.3
$W(\to e\nu) + b\bar{b}$	23.6
$W + heavy\ flavor$	32.8
WZ	1.1
$Z(\to e^+e^-)$	0.5
$Z(\to e^+e^-) + b\bar{b}$	0.6
Total Physics Backgrounds	88.5
Instrumental Backgrounds:	
QCD-multijet	16.3
W + jets mistag	10.3
Total Background:	115.1

TABLE II: Estimated event yields in our final data set.

Instrumental backgrounds arise from events in which objects are misreconstructed or misidentified. The QCD-multijet background is due to events with jets in which one or more jets are poorly measured, resulting in a substantial amount of missing momentum, and another jet fakes the electron signature.

The W+jets background originates from events in which a light-quark or gluon jet is falsely identified as a b-jet. This contribution is estimated from the untagged W+jets data sample.

The expected background event yields are listed in Table II.

We use a parameterized Monte Carlo simulation, interfaced with PYTHIA 6.224 to simulate $W\pi_T$ signal events. The simulation was tuned to reproduce the kinematic distributions and acceptances from fully simulated Monte Carlo events. The cross sections were calculated as a function of the mass parameters M_V while other parameters of the theory were held at suggested default values [1]. The branching ratio for $W \to e\nu = 0.1068$ has been used to calculate cross sections. CTEQ5L parton distribution functions were used. We also use a multiplicative K-factor whose value depends upon the strong coupling constant α_s which itself depends upon the momentum transfer, Q^2 at the collision. For Q^2 of the order of the ρ_T mass of few hundred GeV, the value of K can be considered constantly equal to 1.3 and is used for this analysis.

We generate events with ρ_T masses between 155 GeV up to a maximum of 220 GeV. The π_T mass values start from the kinematic threshold for $W\pi_T$ production at $m_{\pi_T} = m_{\rho_T} - m_W$ up to $m_{\pi_T} = m_{\rho_T}/2$ where the decay channel $\rho_T^{\pm(0)} \to \pi_T^{\pm,(0,\pm)}\pi_T^{0,(0,\mp)}$ becomes accessible with the consequence of reducing the branching ratio of $\rho_T^{\pm(0)} \to W\pi_T$. We set $m_{\omega_T} = m_{\rho_T}$ as suggested by the TCSM2 authors.

Topological variables used for Signal Separation

The technicolor particles are expected to have narrow widths (≈ 1 GeV). We should therefore see enhancement in the distributions of dijet invariant mass $M(jj)$ and the invariant mass of the W boson-dijet system $M(Wjj)$.

We use the following kinematic variables to discriminate between signal and background.

- $\Delta\phi(j,j)$ is the difference in ϕ between the two jets in the event.
- $\Delta\phi(e,\not{p}_T)$ is difference in ϕ between the electron and the missing transverse momentum;
- $p_T(jj)$ is the transverse momentum of the dijet system.
- H_T^e is the scalar sum of p_T of the electron and the two jets in the event.
- $M(j,j)$ is the invariant mass of the dijet system. This corresponds to the reconstructed π_T mass.
- $M(Wjj)$ is the invariant mass of the W boson-dijet system. This corresponds to the reconstructed ρ_T mass. We reconstruct the W boson from the electron and the missing transverse momentum using the W mass constraint

to solve for p_z of the neutrino. If there are two real solutions, we take the smaller value of neutrino p_z. If there is only a complex solution, we take the real part.

Distributions for these variables are shown in Figures 1, 2 and 3. We use two approaches to separate signal and background, a cut based analysis and a neural network analysis.

Cut-Based Analysis

The cut-based analysis was optimized using Monte Carlo simulations to maximize the ratio $S/\sqrt{B}$ for every set of techni-particle masses. S is the expected number of $W\pi_T$ events and B is the expected number of background events. For each topological variable, the $S/\sqrt{B}$ ratio as a function of the value of the variable is examined to determine a set of lower, upper or window cuts which maximizes this ratio. For one particular mass point, $M(\rho_T) = 210$ GeV and $M(\pi_T) = 110$ GeV, the cut flow is shown extensively in Fig. 4. In this figure, after baseline cuts the distribution for H_T^e for signal, SM prediction and data are shown, together with the the optimized window cut on the H_T^e variable. The distribution for $\Delta\phi(e, MET)$ is shown after cuts on the H_T^e variable. The variable $\Delta\phi(jj)$ is plotted after optimized cut on $\Delta\phi(e, MET)$ from the previous step. The $p_T(jj)$, $M(Wjj)$ and $M(jj)$ distributions are displayed after cuts on the previous three variables (H_T^e, $\Delta\phi(e, MET)$, and $\Delta\phi(jj)$). As we expect to see two simultaneous signals due to the production of ρ_T and π_T in this search, we also plot the distribution of the correlation between $M(Wjj)$ and $M(jj)$ for $W\pi_T$ signal, background and data after cuts on H_T^e, $\Delta\phi(e, MET)$, and $\Delta\phi(jj)$ in Fig. 6. In Figures 7 and 8, the number of data, background and signal events are shown after all cuts on the kinematic variables, including a cut on a mass window appropriately chosen for the particular ρ_T and π_T mass combination being investigated.

Neural Network Based Analysis

The neural network analysis uses the topological variables H_T^e, $\Delta\phi(e, MET)$, and $\Delta\phi(jj)$ $p_T(jj)$, the transverse momenta of both jets and the electron, and the missing transverse momentum, which are shown in Fig. 9. A two-stage neural network based on the Multi Layer Perceptron algorithm is used. The layout of the first stage of this network consists of 8 input nodes and one hidden layer with 24 nodes, while the second stage has 3 input nodes and one hidden layer with 6 nodes. The inputs to the first stage of the network are the topological variables described above, This first stage consists of three independent networks which represent the different types of backgrounds. These are the Wjj network (includes both light quark and heavy flavor events), $Wb\bar{b}$ network, and the top network (includes the $t\bar{t}$ and single top events). The output distributions for different background samples when we apply one of the three first stage networks (Wjj) are shown in Fig. 10. To train the network for the second stage, the three individual networks of the first stage are applied to each of the nine different physics backgrounds. For a given network from the first stage, these nine backgrounds are combined by weighting their respective contributions by the expected number of events as listed in Table II. The signal and background output distributions for each of the three first stage networks are then used as the inputs to the second stage network. The output of the second stage neural network (Super NN) for each of the physics background considered are displayed in Fig. 11.

We apply the neural network to the collider data, technicolor signals, physics and instrumental backgrounds to obtain the discriminator output spectra, Fig. 12 (left plot). We optimize the discriminator cut for every set of techniparticle masses to maximize $S/\sqrt{B}$, shown for one mass point in Fig. 12 (right plot). The correlation of $M(Wjj)$ and $M(jj)$ for the data, the $W\pi_T$ signal ($M(\rho_T) = 200$ GeV, $M(\pi_T) =$ 105 GeV), and the backgrounds after the discriminator cut and weighting them with the neural network discriminator output is shown in Fig. 13. The data along with expected backgrounds after applying the NN discriminant cut as determined from the $S/\sqrt{B}$ optimization for each point on the grid, is presented in Figures 14 and 15.

Systematic Uncertainties

The systematic uncertainties are shown in Table III. The uncertainties are estimated by evaluating the variation of signal and background after each set of cuts. In this table the systematic uncertainty quoted for the Neural Network itself is estimated by examining the outputs of the different training trials.

Uncertainty Source	Signal		Background	
	NN	cut-based	NN	cut-based
Jet Resolution	9.3%	4.0%	0.4%	1.9%
Jet Energy Scale	11.7%	4.5%	3.1%	1.8%
Jet Efficiency	7.2%	4.8%	4.2%	6.6%
b-tag	6.2%	1.6%	1.3%	1.5%
electron ID	1.5%	4.0%	1.5%	4.0%
PMCS	5.4%	5.4%	-	-
NN	5 %	-	5%	-
Cross Section	-	-	6%	3.7%
Background modeling	4%	-	4%	3.4%

TABLE III: Summary of systematic uncertainties for signal and background.

95% C.L. Upper Limit on the Cross Section

In the absence of an excess over the expected background, we compute a 95% confidence level upper limit on the $\rho_T \to W\pi_T \to e\nu\ b\bar{b}(\bar{c})$ production cross section times branching ratio. In the cut-based analysis, which is a simple counting experiment, the limits are computed using Bayesian statistics [15]. The neural network analysis uses a 2-dimensional binned maximum likelihood technique to estimate the number of technicolor signal events by constraining the physics backgrounds and instrumental background contributions to the respective expectations within the statistical and systematic uncertainties. The 2-D mass histograms for computing the binned maximum likelihood is the one shown in Fig. 13. Figure 16 shows the maximum likelihood distribution as a function of the number of expected technicolor signal events for mass $M(\rho_T) = 200$ GeV and $M(\pi_T) = 105$ GeV for the observed data (left plot) and in the case where the observed events are modeled by the expected SM background (right plot). The arrows on left (right) plot indicates the number of observed (expected) technicolor events for a 95% C.L. upper limit. To estimate the excursions of these upper limits, pseudo experiments are performed using the variation of systematic and statistical uncertainty. The observed and expected 95% C.L. upper limits from these experiments are presented respectively as the left and right plots of Fig. . The red superposed histograms indicate the 95% C.L. upper limits on observed and expected cross section.

The overall sensitivity and the regions excluded at 95% confidence level by both the cut-based and the neural network analyses in the M_{ρ_T}, M_{π_T} plane, for $M_V = 500$ GeV are illustrated in Figures 18, 19 and 20 and listed in Tables IV through VI. We exclude a much smaller region for $M_V = 100$ GeV as shown in Table. V.

$M(\rho_T)$	$M(\pi_T)$ excluded region at 95% C.L. (NN) $M_V = 500$ GeV	$M(\pi_T)$ excluded region at 95% C.L.(Topo)
170 GeV	$83 \leq M(\pi_T) \leq 87$ GeV	
175 GeV	$86 \leq M(\pi_T) \leq 92$ GeV	
180 GeV	$87 \leq M(\pi_T) \leq 95$ GeV	$89.7 \leq M(\pi_T) \leq 90.4$ GeV
185 GeV	$90 \leq M(\pi_T) \leq 99$ GeV	$92.6 \leq M(\pi_T) \leq 97.1$ GeV
190 GeV	$93 \leq M(\pi_T) \leq 103$ GeV	$91.8 \leq M(\pi_T) \leq 102.2$ GeV
195 GeV	$93 \leq M(\pi_T) \leq 107$ GeV	$96.7 \leq M(\pi_T) \leq 107.4$ GeV
200 GeV	$97 \leq M(\pi_T) \leq 113$ GeV	$96.8 \leq M(\pi_T) \leq 111.6$ GeV
205 GeV	$103 \leq M(\pi_T) \leq 115$ GeV	$99.0 \leq M(\pi_T) \leq 114.9$ GeV
210 GeV	$105 \leq M(\pi_T) \leq 120$ GeV	$101.9 \leq M(\pi_T) \leq 115.0$ GeV
215 GeV	110 GeV	$107.2 \leq M(\pi_T) \leq 115.0$ GeV

TABLE IV: Excluded region at 95% C.L. in the $(M(\rho_T), M(\pi_T))$ plane for $\rho_T \to W\pi_T \to e\nu\ b\bar{b}(\bar{c})$ production with $M_V = 500$ GeV calculated using 388 pb $^{-1}$ of DØ data and compared with the excluded region from topological analysis.

$M(\rho_T)$	$M(\pi_T)$ excluded region at 95% C.L. (NN) $M_V = 100$ GeV	$M(\pi_T)$ excluded region at 95% C.L. (Topo)
185 GeV	95 GeV	
190 GeV	95 GeV	$95 \leq M(\pi_T) \leq 96$ GeV
200GeV		$100 \leq M(\pi_T) \leq 105$ GeV

TABLE V: Excluded region at 95% C.L. in the $(M(\rho_T), M(\pi_T))$ plane for $\rho_T \to W\pi_T \to e\nu\ b\bar{b}(\bar{c})$ production with $M_V = 100$ GeV calculated using 388 pb $^{-1}$ of DØ data and compared with the excluded region from topological analysis.

$M(\rho_T)$	$M(\pi_T)$ excluded region at 95% C.L. (NN) $M_V = 500$ GeV	$M(\pi_T)$ excluded region at 95% C.L.(Topo)
170 GeV	$82 \leq M(\pi_T) \leq 87$ GeV	$83.3 \leq M(\pi_T) \leq 86.7$ GeV
175 GeV	$85 \leq M(\pi_T) \leq 93$ GeV	$88.1 \leq M(\pi_T) \leq 91.5$ GeV
180 GeV	$87 \leq M(\pi_T) \leq 97$ GeV	$88.1 \leq M(\pi_T) \leq 96.0$ GeV
185 GeV	$90 \leq M(\pi_T) \leq 102$ GeV	$92.1 \leq M(\pi_T) \leq 98.8$ GeV
190 GeV	$93 \leq M(\pi_T) \leq 105$ GeV	$94.0 \leq M(\pi_T) \leq 101.4$ GeV
195 GeV	$95 \leq M(\pi_T) \leq 110$ GeV	$98.3 \leq M(\pi_T) \leq 106.7$ GeV
200 GeV	$97 \leq M(\pi_T) \leq 114$ GeV	$99.5 \leq M(\pi_T) \leq 110.0$ GeV
205 GeV	$102 \leq M(\pi_T) \leq 117$ GeV	$104.4 \leq M(\pi_T) \leq 112.1$ GeV
210 GeV	$104 \leq M(\pi_T) \leq 120$ GeV	
215 GeV	$110 \leq M(\pi_T) \leq 125$ GeV	
220 GeV	$115 \leq M(\pi_T) \leq 126$ GeV	

TABLE VI: Expected excluded region at 95% C.L. in the $(M(\rho_T), M(\pi_T))$ plane for $\rho_T \to W\pi_T \to e\nu\ b\bar{b}(\bar{c})$ production with $M_V = 500$ GeV calculated using 388 pb $^{-1}$ of DØ data and compared with the excluded region from topological analysis.

$M(\rho_T)$	$M(\pi_T)$ expected excluded region at 95% C.L. (NN) $M_V = 100$ GeV
170 GeV	85 GeV
175 GeV	90 GeV
180 GeV	$88 \leq M(\pi_T) \leq 93$ GeV
185 GeV	$94 \leq M(\pi_T) \leq 98$ GeV
190 GeV	95 GeV

TABLE VII: Expected excluded region at 95% C.L. in the $(M(\rho_T), M(\pi_T))$ plane for $\rho_T \to W\pi_T \to e\nu\ b\bar{b}(\bar{c})$ production with $M_V = 100$ GeV calculated using 388 pb $^{-1}$ of DØ data. No expected exclusion region for the topological analysis.

[*] On leave from IEP SAS Kosice, Slovakia.
[†] Visitor from Helsinki Institute of Physics, Helsinki, Finland.

[1] K. Lane and S. Mrenna, "The Collider Phenomenology of Technihadrons in the Technicolor Straw Man Model", Phys. Rev. D**67**, 115011 (2003).
[2] S. Weinberg, "Implication of Dynamical Symmetry Breaking", Phys. Rev. D **974**, 13 (1976)
[3] L. Susskind, "Dynamics of Spontaneous Symmetry Breaking in the Weinberg-Salam Theory", Phys. Rev. D **2619**, 20 (1979)
[4] S. Dimopoulos and L. Susskind, "Mass without scalars", Nucl. Phys. B **237**, 155
[5] E. Eichten and K. Lane, "Dynamical Breaking of Weak Interaction Symmetries", Phys. Lett. B **125**, 90
[6] B. Holdom, "Raising the sideways scale", Phys. Lett. D **1441**, 24 (1981)
[7] C. T. Hill, "Topcolor Assisted Technicolor", Phys. Lett. B **274**, 222 (1989)
[8] E. Eichten, K. Lane and J. Womersley, Phys. Lett. **305**, B 405 (1997).
[9] K. Lane, Frascati Spring School, *Technicolor 2000*, Frascati, RM Italy, 2000.
[10] V. M. Abazov *et al.*, "The Upgraded DØ Detector", accepted by Nucl. Instr. and Methods, physics/0507191, Fermilab-Pub-05/341-E.
[11] DØ note 4796, D. Boline *et al.*, "Update on b-quark identification with Secondary Vertex reconstruction using p14-pass2 Sample".
[12] R. Brun and F. Carminati, CERN Program Library Long Writeup W5013, 1993 (unpublished).
[13] T. Sjöstrand *et al.*, Comput. Phys. Commun. **135**, 238 (2001).
[14] F. Caravaglios, M. L. Mangano, M. Moretti, R. Pittau, "A new approach to multijet calculations in hadron collisions", Nucl. Phys. B **539** 215-232 (1999).
[15] I. Bertram *et al.*, FERMILAB-TM-2104 (2000).

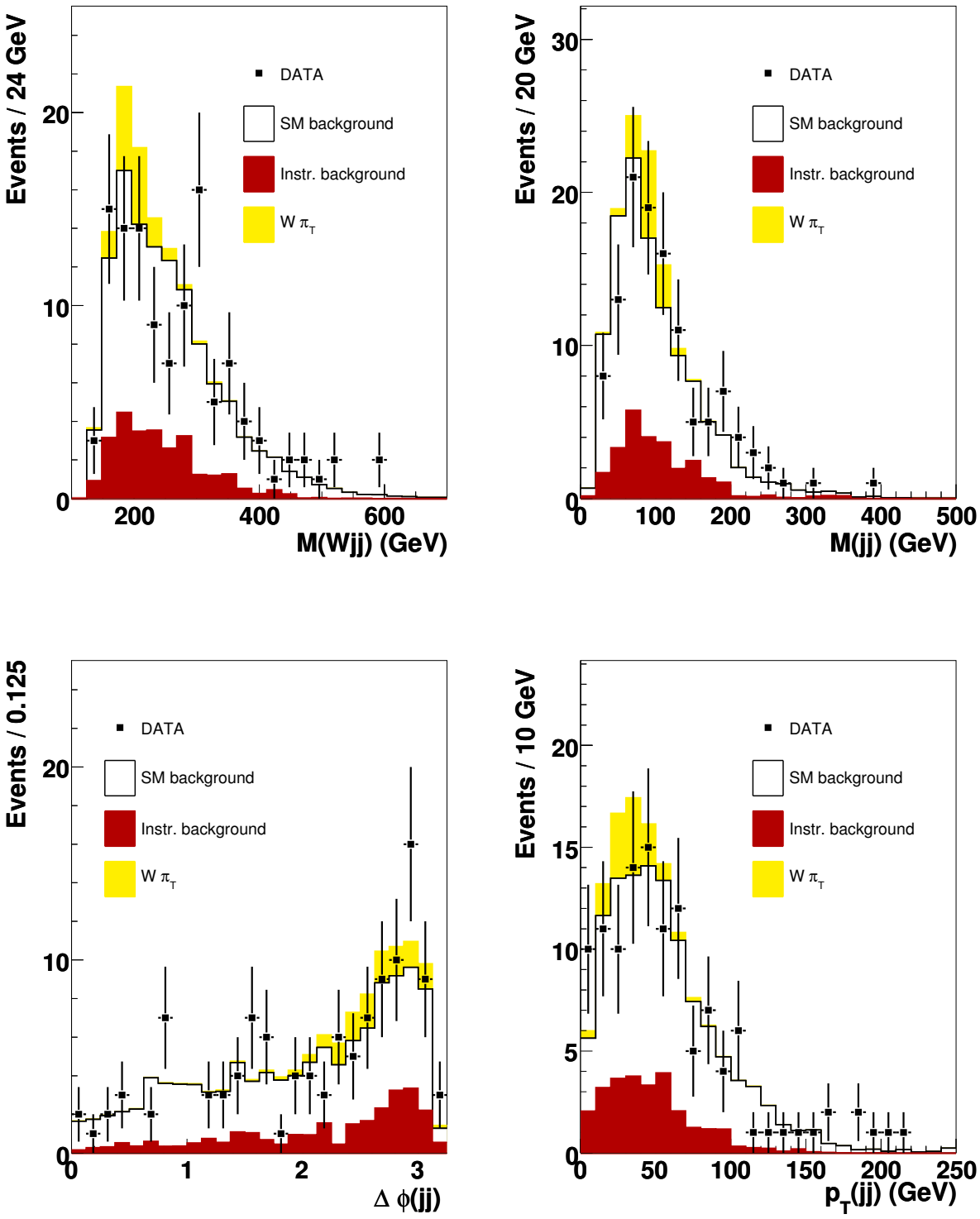

FIG. 1: Distribution for topological variables used for cut-based and NN analysis after W + 2 jets $\geq$ 1 b-tag selection. The white histogram represents the Standard Model prediction, red solid histogram represents the instrumental background, the yellow histogram is the predicted $W\pi_T$ signal for $M(\rho_T) = 210$ GeV and $M(\pi_T) = 110$ GeV. Black dots are data.

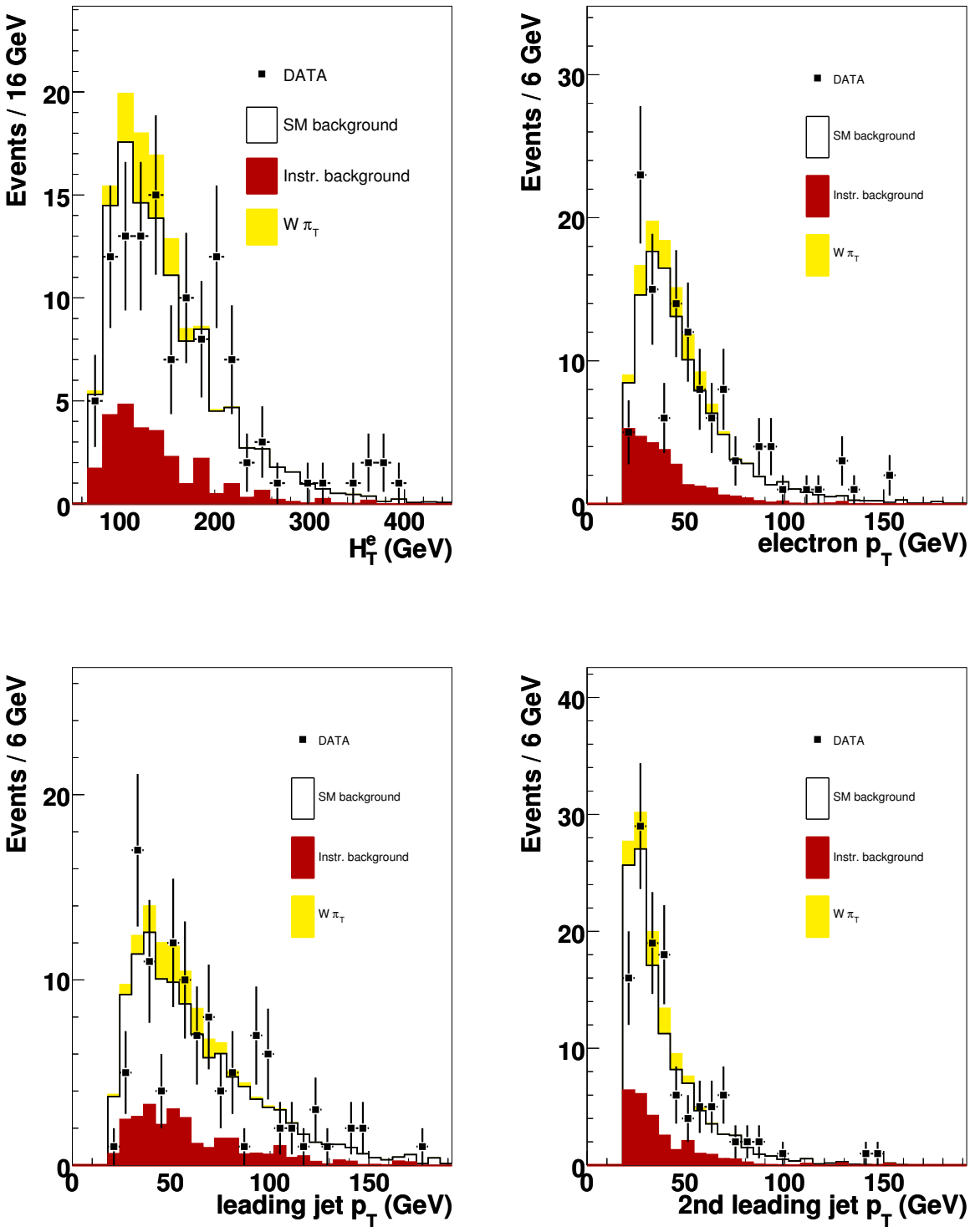

FIG. 2: Distribution for topological variables used for cut-based and NN analysis after W + 2 jets $\geq$ 1 b-tag selection. The white histogram represents the Standard Model prediction, red solid histogram represents the instrumental background, the yellow histogram is the predicted $W\pi_T$ signal for $M(\rho_T) = 210$ GeV and $M(\pi_T) = 110$ GeV. Black dots are data.

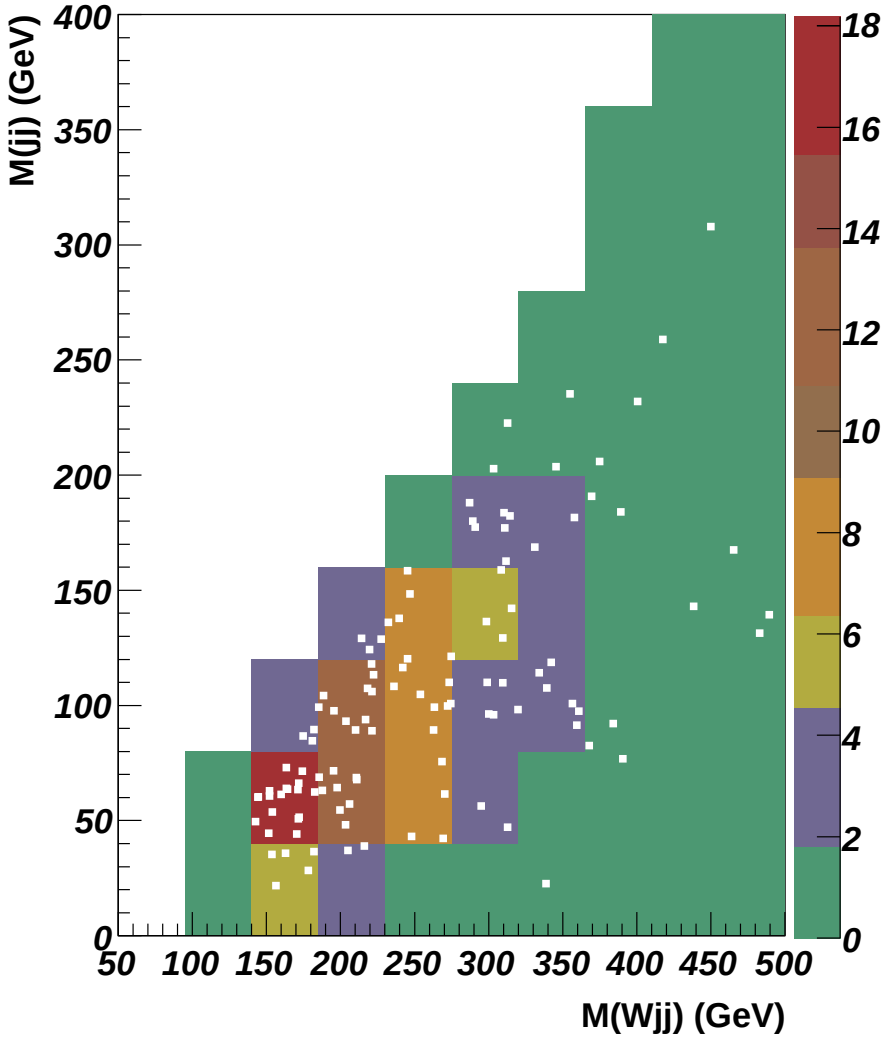

FIG. 3: Distributions for $M(jj)$ versus $M(Wjj)$. The colored 2D histogram represents the expected SM background and the white squares represent data after $W + 2\ jets \geq 1b\text{-}tag$ selection.

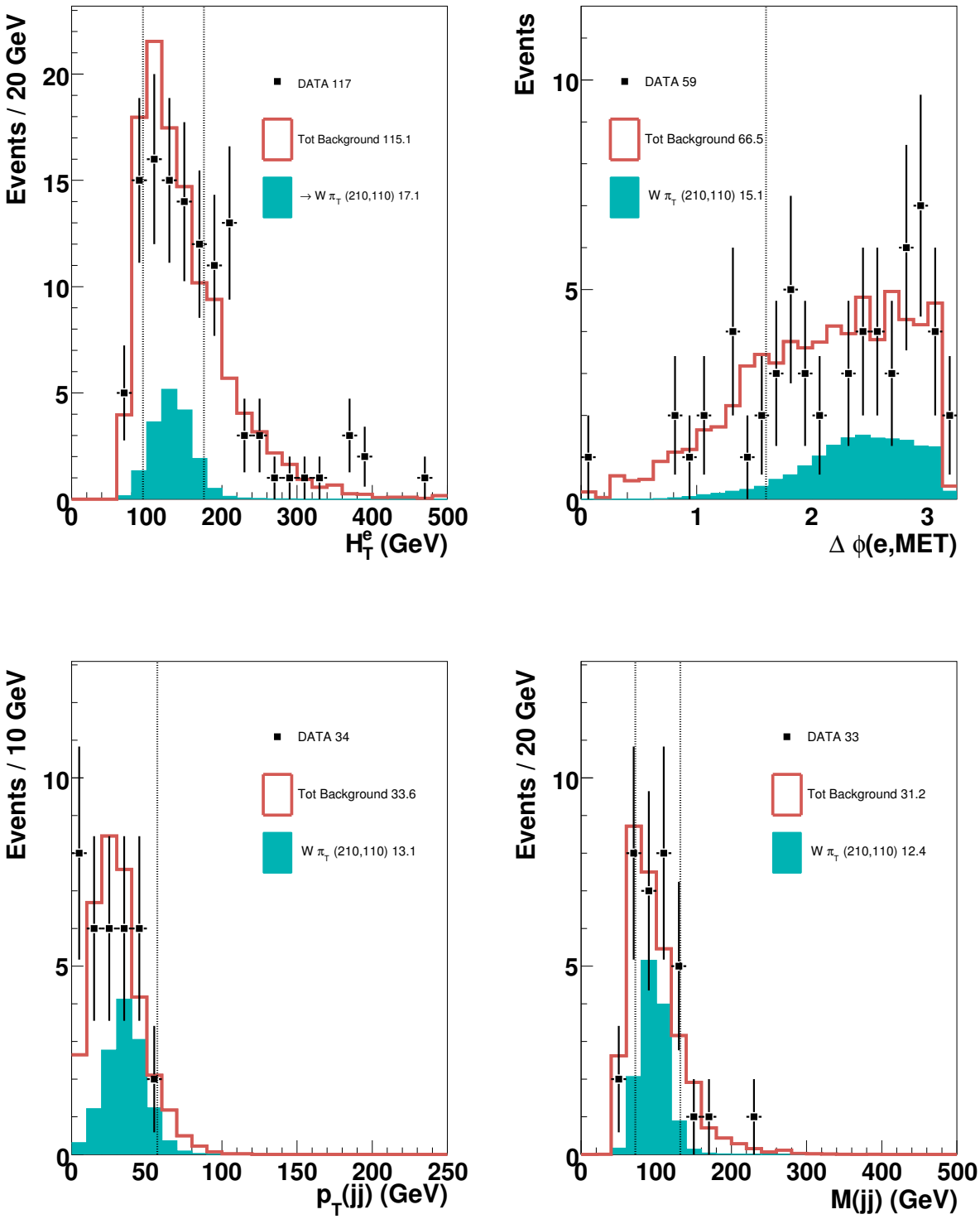

FIG. 4: Distributions for H_T^e (top left), $\Delta\phi(e, MET)$ (top right), $p_T(jj)$ (bottom left), $M(jj)$ (bottom right) for $W\pi_T$ produced with $M(\rho_T) = 210$ GeV and $M(\pi_T) = 110$ GeV (azure histogram), SM predicted background (red histogram) and data (black squares). Dotted lines represent the optimized cuts for H_T^e (176 GeV $\leq H_T^e \leq$ 95 GeV), $\Delta\phi(e, MET)$ ($\Delta\phi(e, MET) \geq 1.6$), $p_T(jj)$ ($p_T(jj) \leq 57$ GeV), $M(jj)$ (72 GeV$\leq M(jj) \leq 132$ GeV).

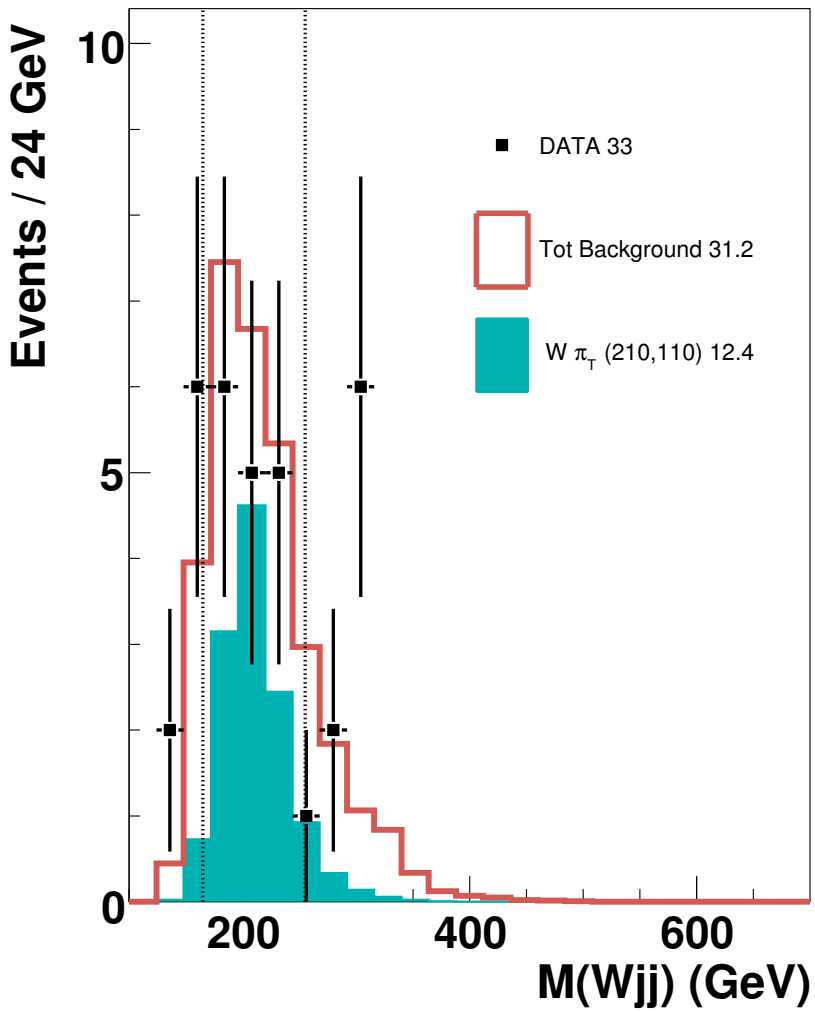

FIG. 5: Distributions for $M(Wjj)$ for $W\pi_T$ produced with $M(\rho_T) = 210$ GeV and $M(\pi_T) = 110$ GeV (azure histogram), SM predicted background (red histogram) and data (black squares). Dotted lines represent the optimized cuts (165 GeV $\leq M(Wjj) \leq 255$ GeV).

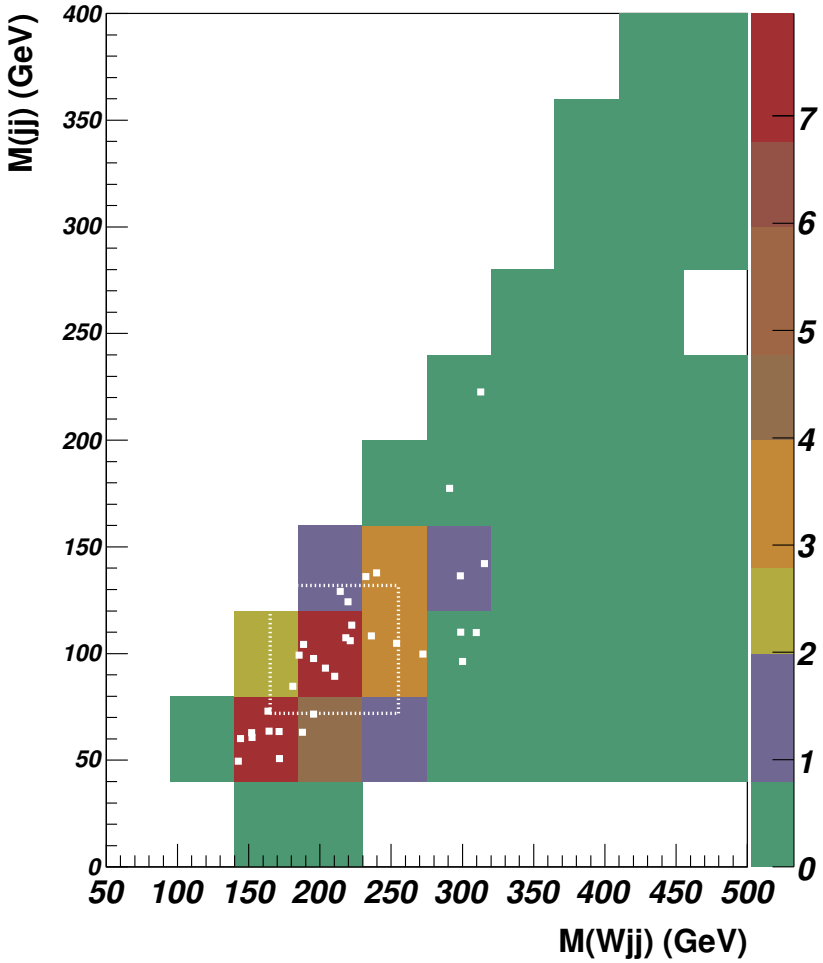

FIG. 6: Distribution of $M(Wjj)$ versus $M(jj)$ for the SM predicted (colored histogram) and data (white dots), after baseline, H_T^e, $\Delta\phi(e, MET)$, $\Delta\phi(jj)$ and $p_T(jj)$ cuts optimized for $W\pi_T$ produced with $M(\rho_T) = 210$ GeV and $M(\pi_T) = 110$ GeV. The optimized mass window cuts are represented with a white dotted line.

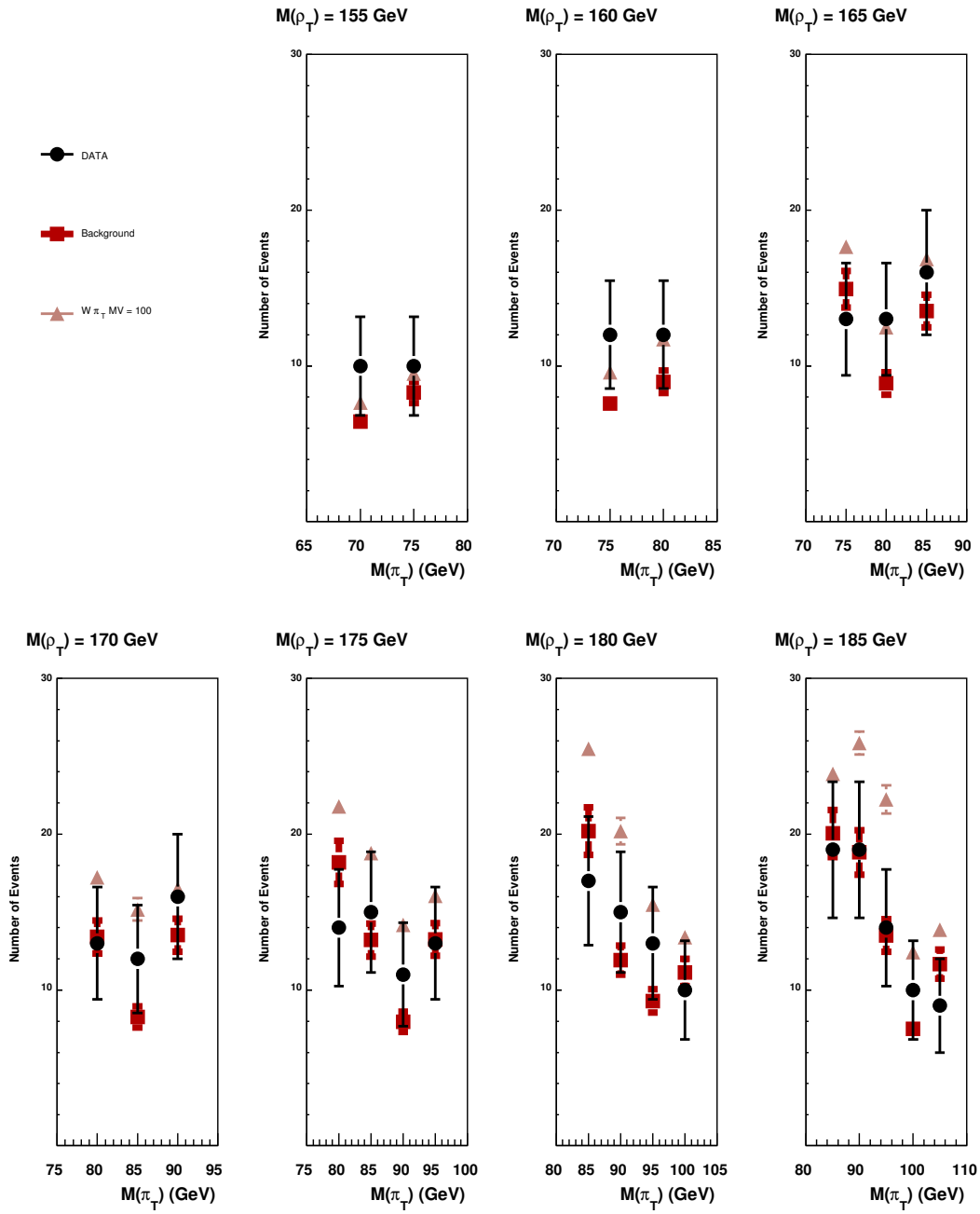

FIG. 7: Comparison of data (black dots) and background (red squares) after all mass-dependent optimized cuts applied. Also shown is the expected $\rho_T \to W\pi_T \to e\nu\, b\bar{b}(\bar{c})$ signal for $M_V = 100$ GeV (brown triangles).

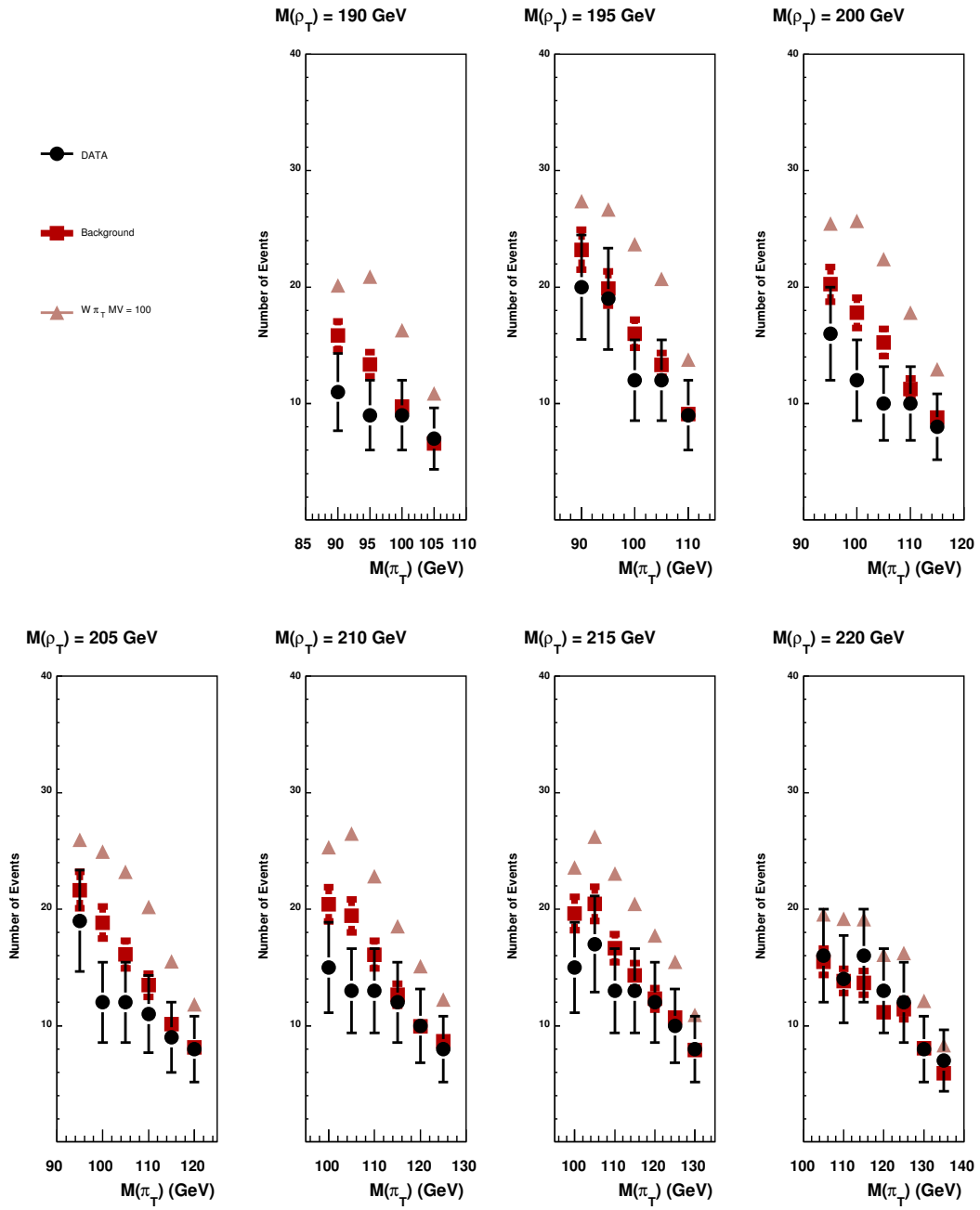

FIG. 8: Comparison of data (black dots) and background (red squares) after all mass-dependent optimized cuts applied. Also shown is the expected $\rho_T \to W\pi_T \to e\nu\, b\bar{b}(\bar{c})$ signal for $M_V = 100$ GeV (brown triangles).

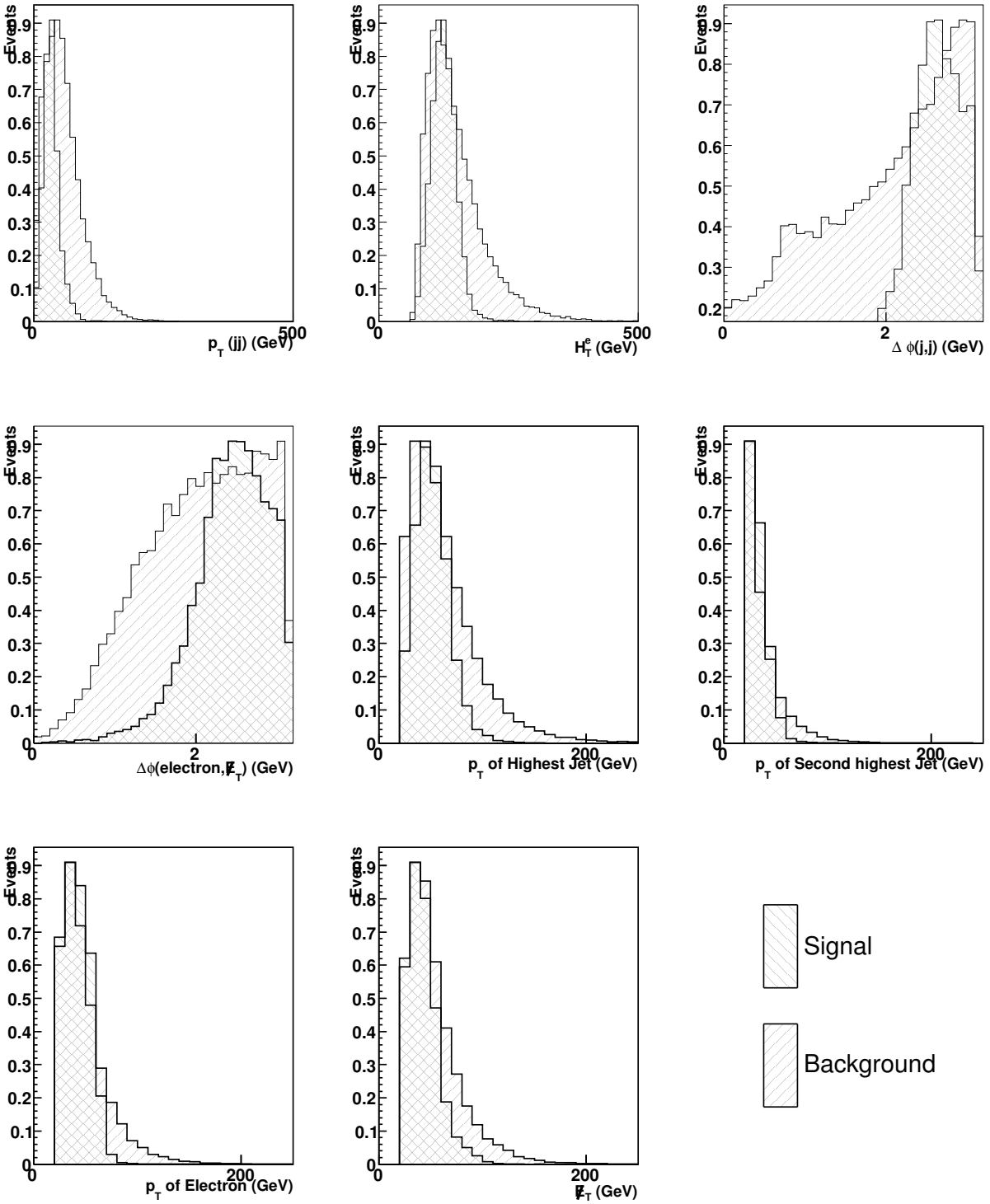

FIG. 9: Input variables for the three first step neural networks (Wjj, Wbb and Top Neural Networks) after $W + 2$ jets ≥ 1 b-tag selection where techniparticle $W\pi_T$ for $M(\rho_T) = 200$ GeV, $M(\pi_T) = 105$ GeV has been used for the signal sample.

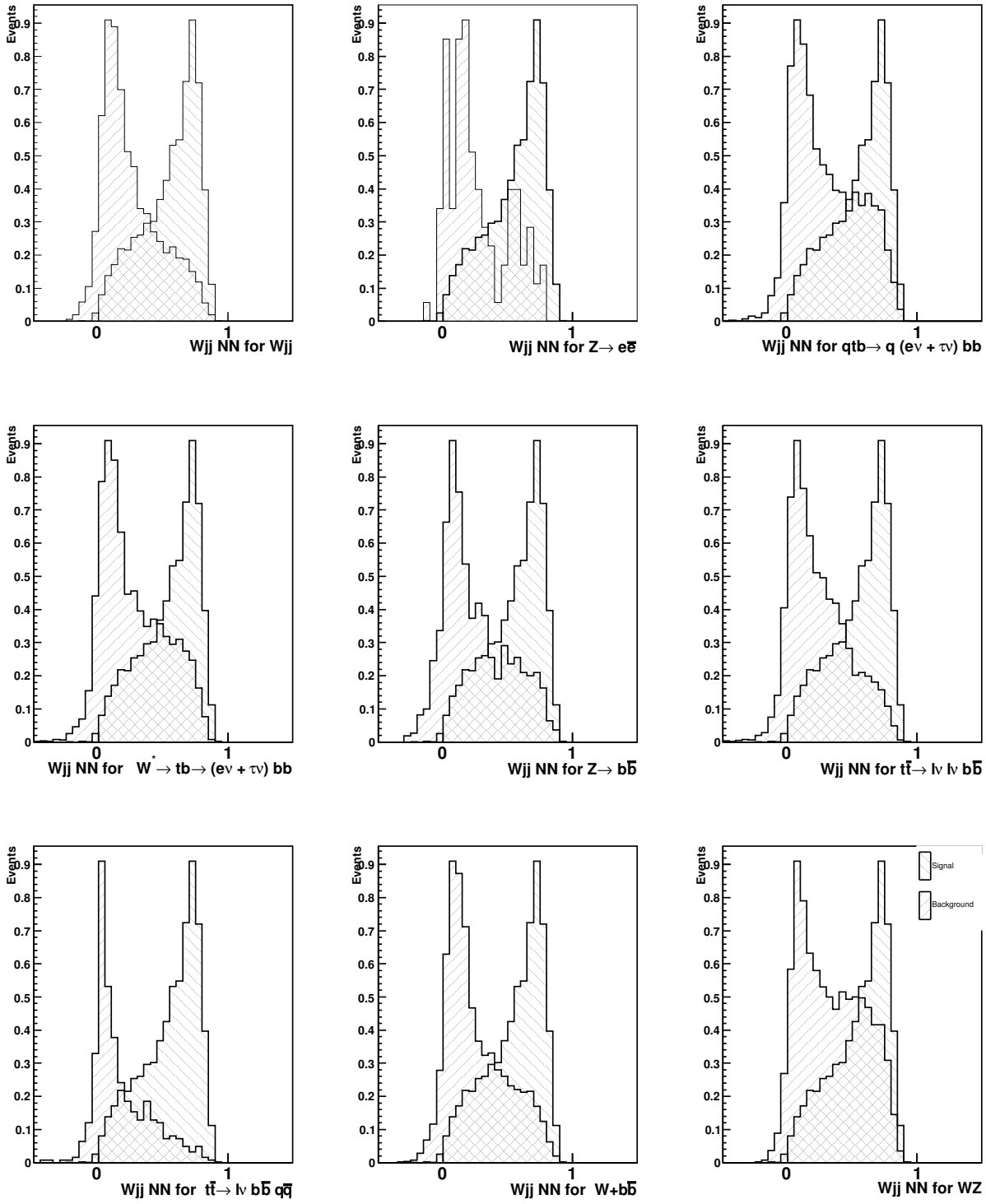

FIG. 10: Output distributions when we apply Wjj Network to each background and signal samples. These distributions are combined to obtain the inputs of the second neural network. Techniparticle $W\pi_T$ for $M(\rho_T) = 200$ GeV, $M(\pi_T) = 105$ GeV has been used for the signal sample. No b-tagging requirement is applied.

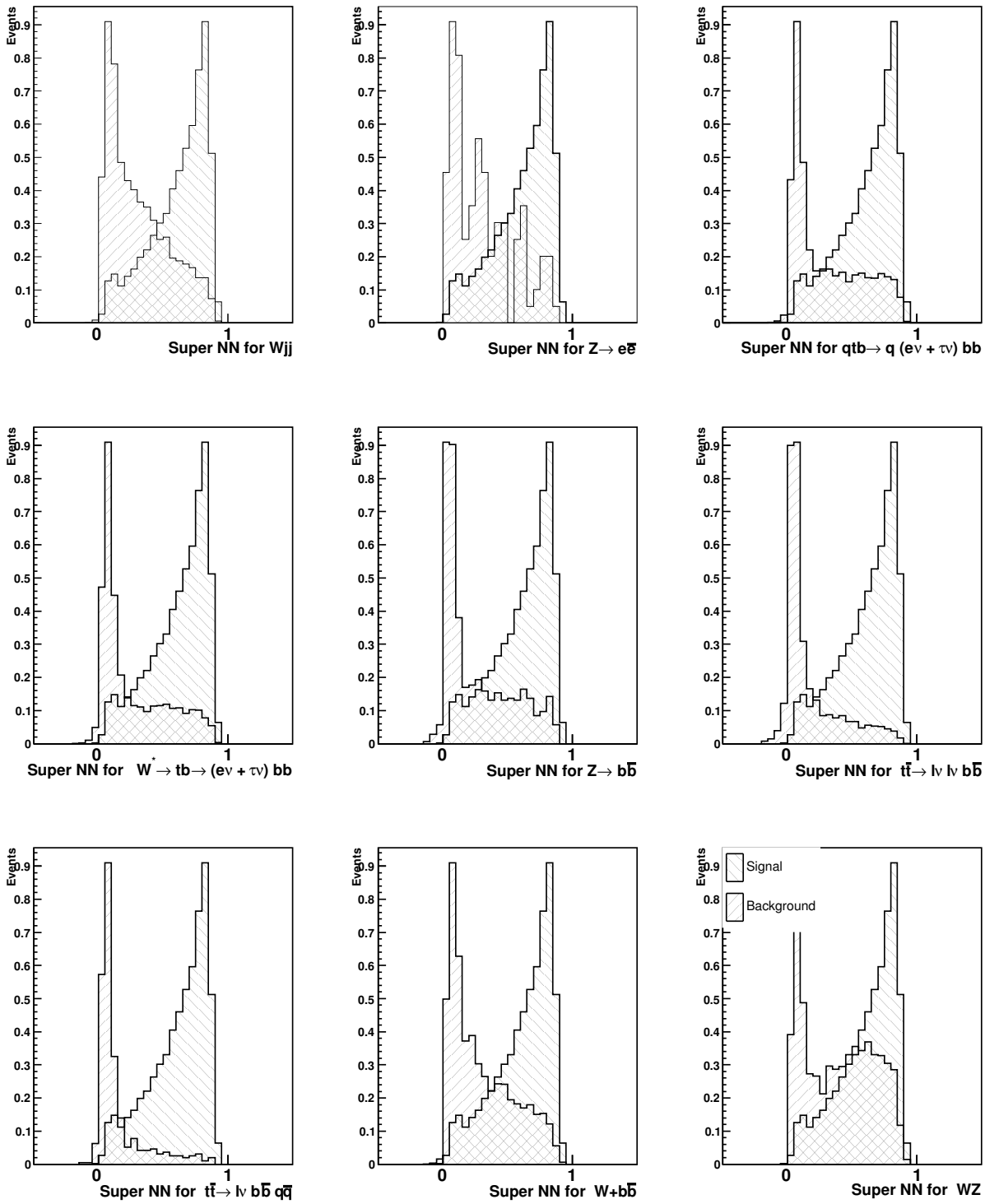

FIG. 11: Output distributions when we apply the second neural network to each of the physics background samples. Techniparticle $W\pi_T$ for $M(\rho_T) = 200$ GeV, $M(\pi_T) = 105$ GeV has been used for the signal sample. No b-tagging requirement is applied.

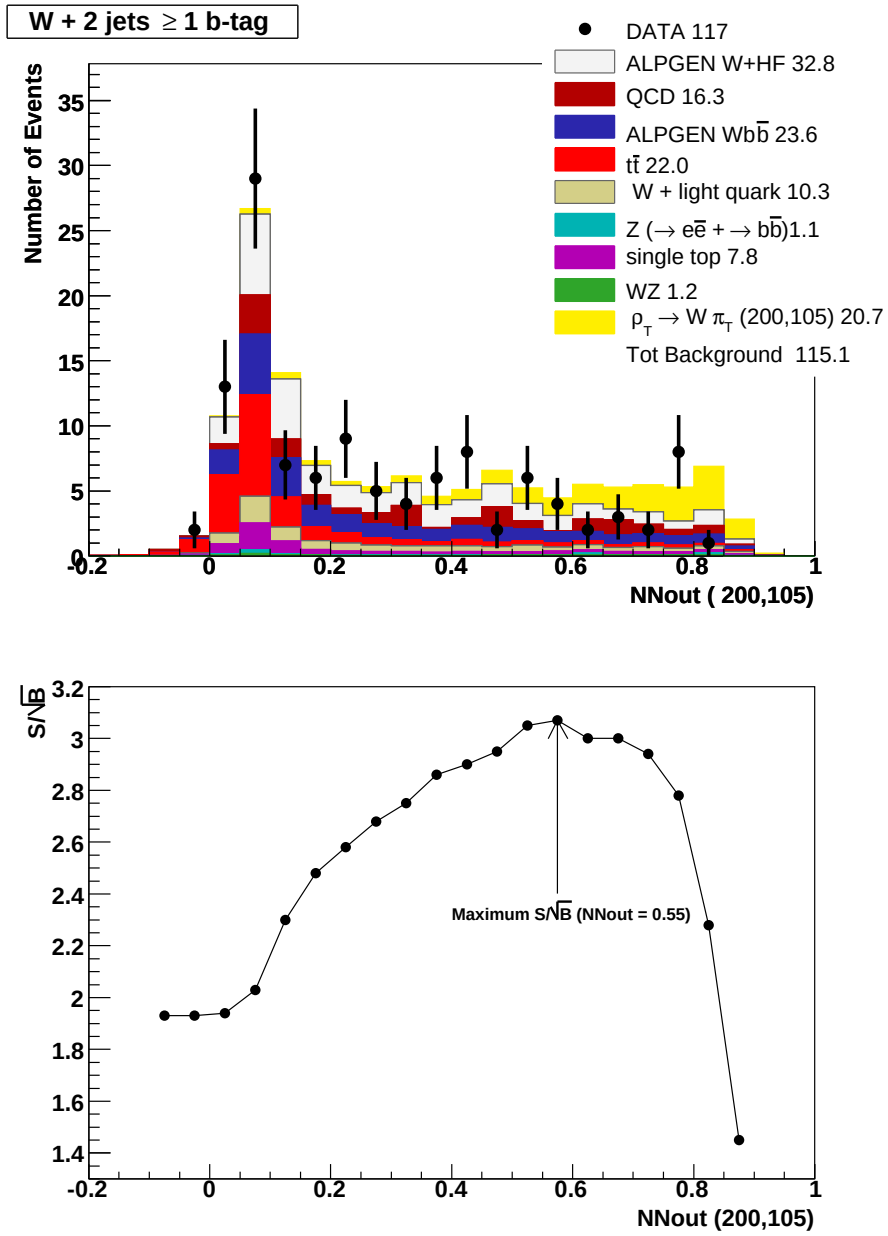

FIG. 12: Distributions of neural network for signal and backgrounds (top) and S/$\sqrt{B}$ as a function of neural network output (bottom). The yellow histogram represents $W\pi_T$ for $M(\rho_T) = 200$ GeV, $M(\pi_T) = 105$ GeV and $M_V = 500$ GeV.

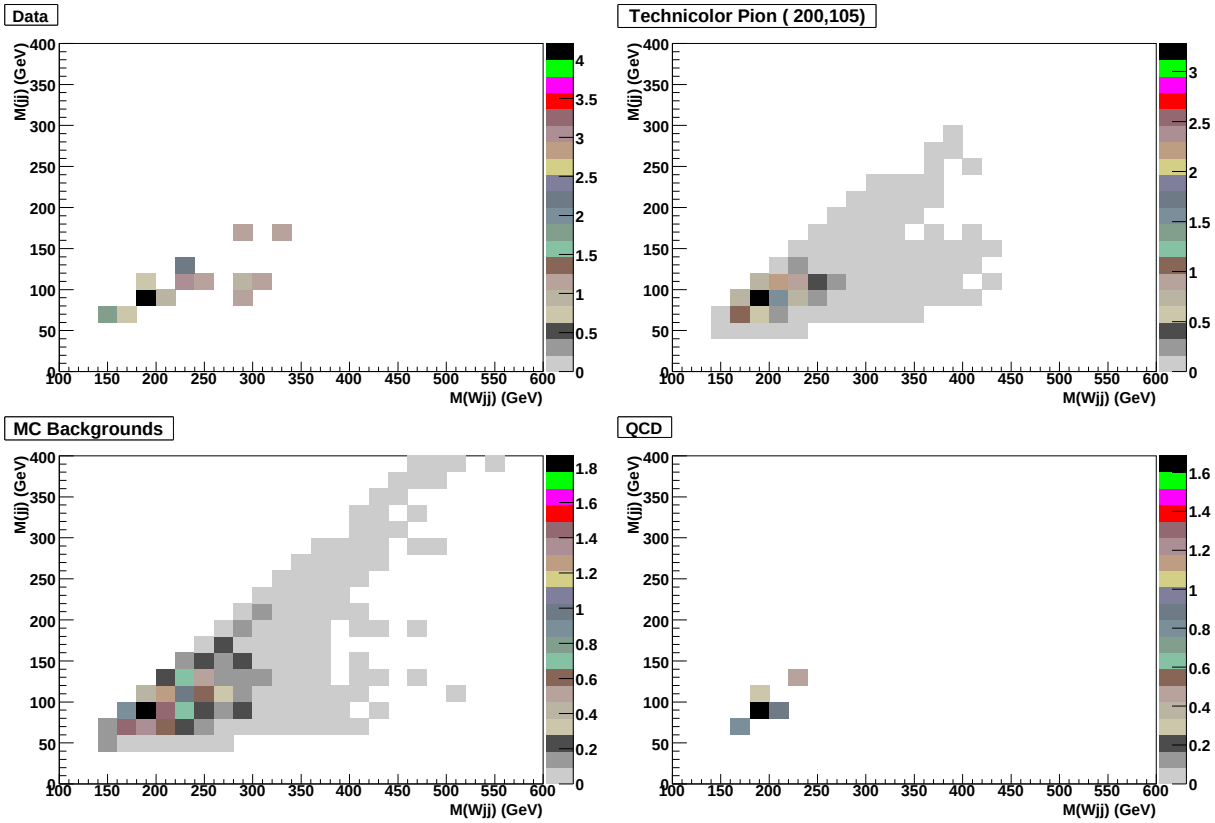

FIG. 13: Distribution of the dijet mass vs $W+$ dijet mass distribution for Data, $\rho_T \to W\pi_T$ ($M(\rho_T) = 200$ GeV, $M(\pi_T) = 105$ GeV, and backgrounds (physics and instrumental) after NN selection. Each event has been reweighted using Super NN information.

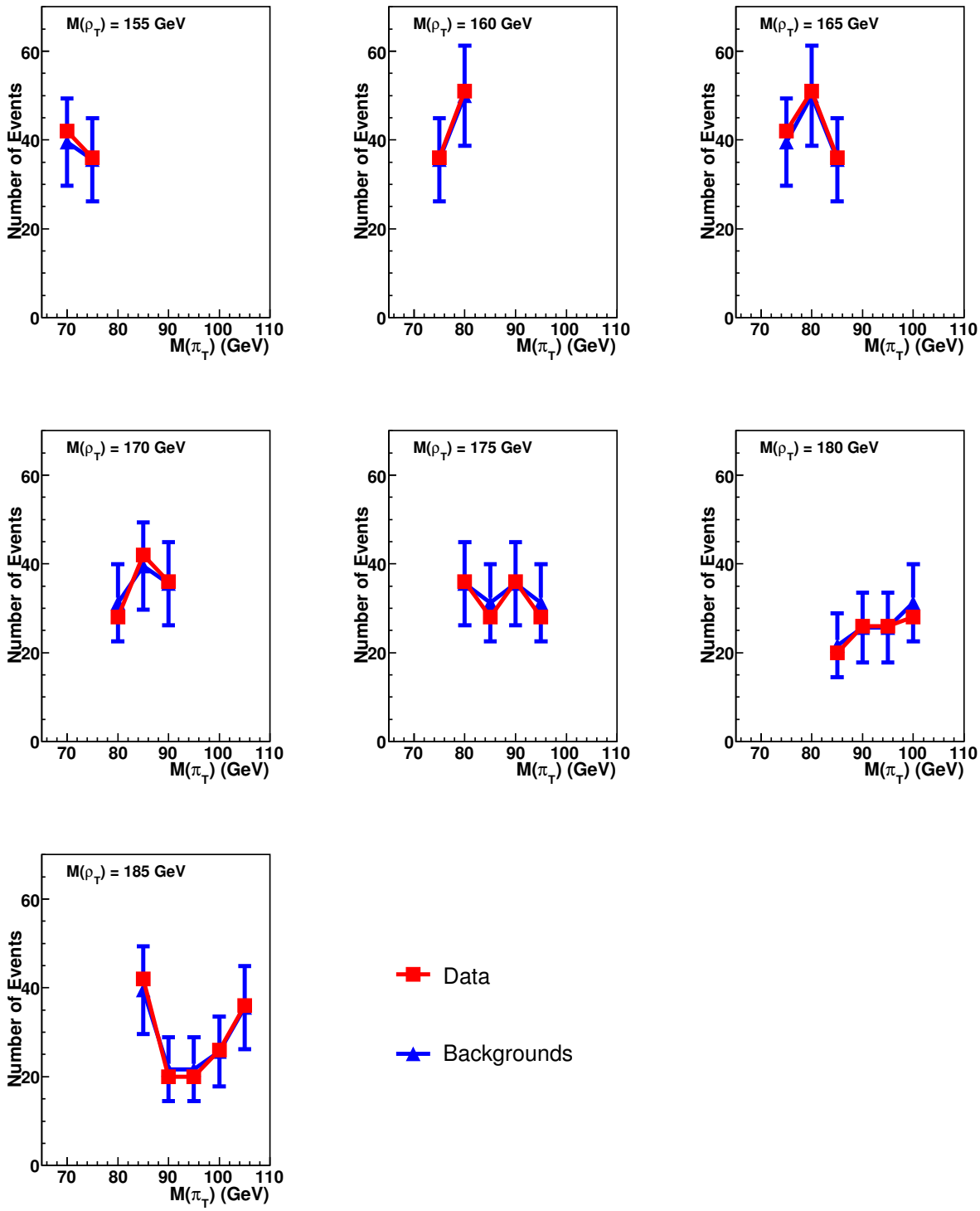

FIG. 14: Comparison of data and background after neural network selection ($NNout$) for the $155 \leq M(\rho_T) \leq 185$ GeV mass grid region.

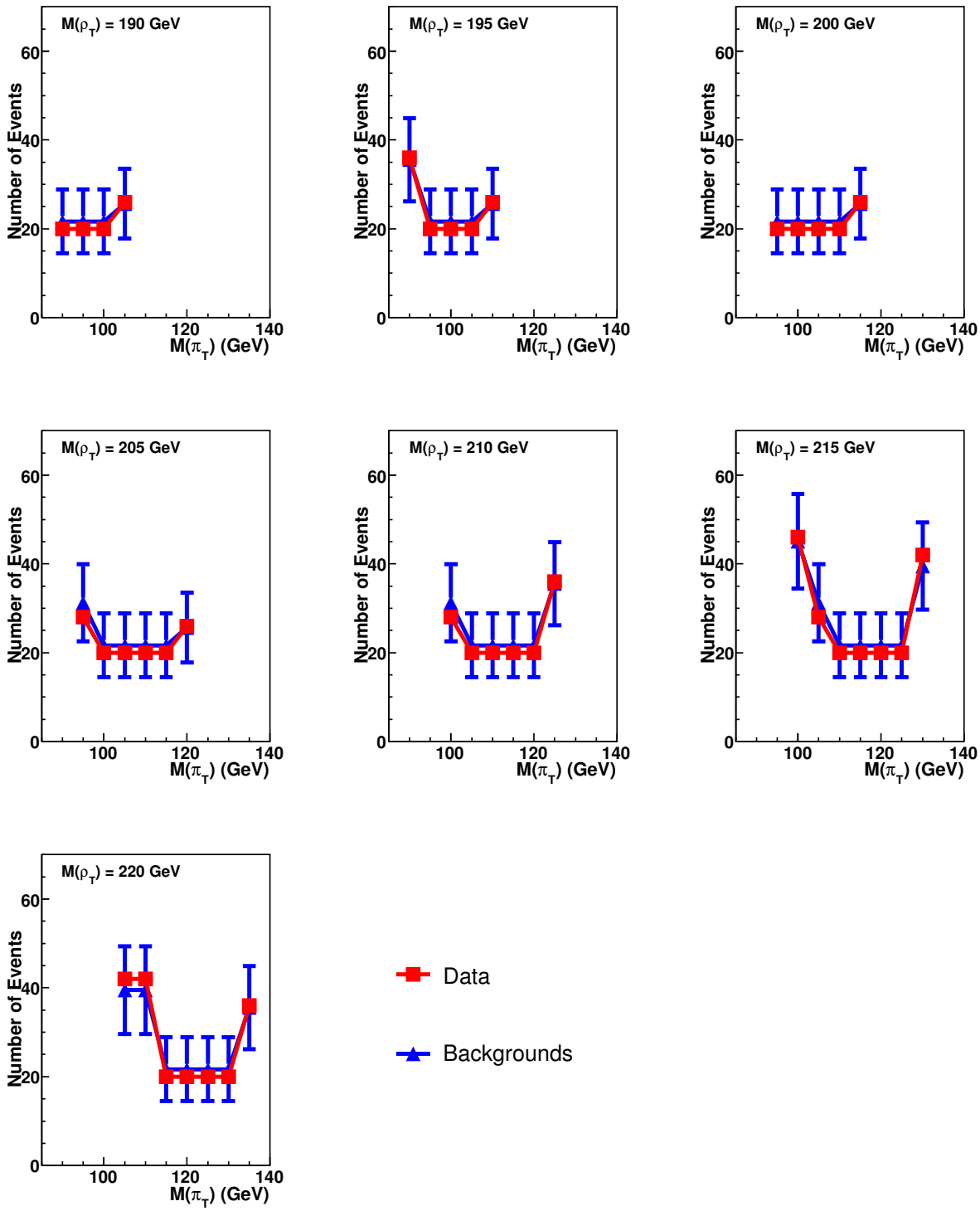

FIG. 15: Comparison of data and background after neural network selection (*nnout*) for the $190 \leq M(\rho_T) \leq 220$ GeV mass grid region.

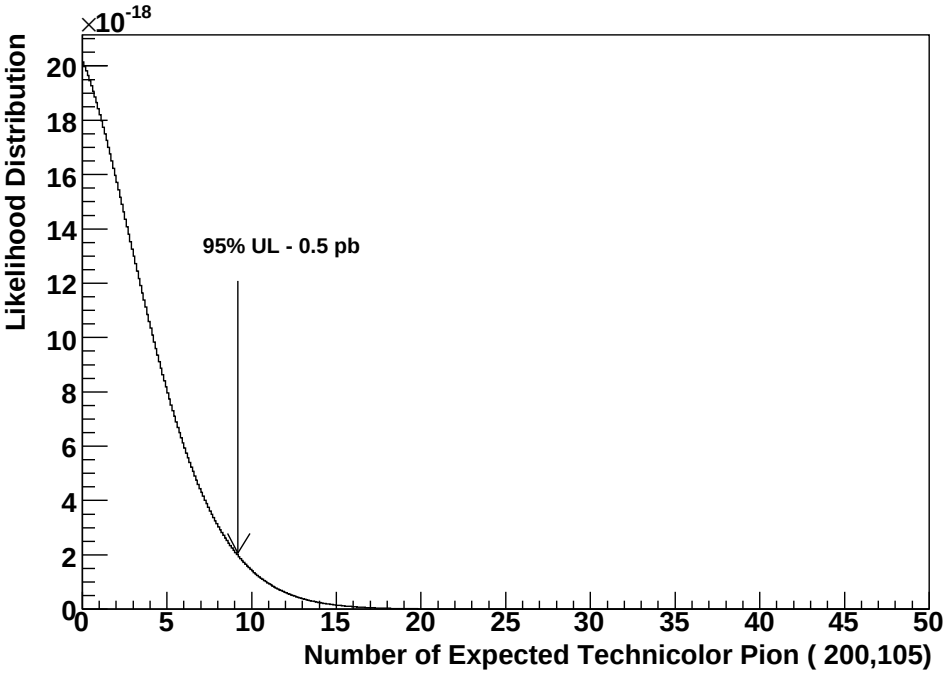

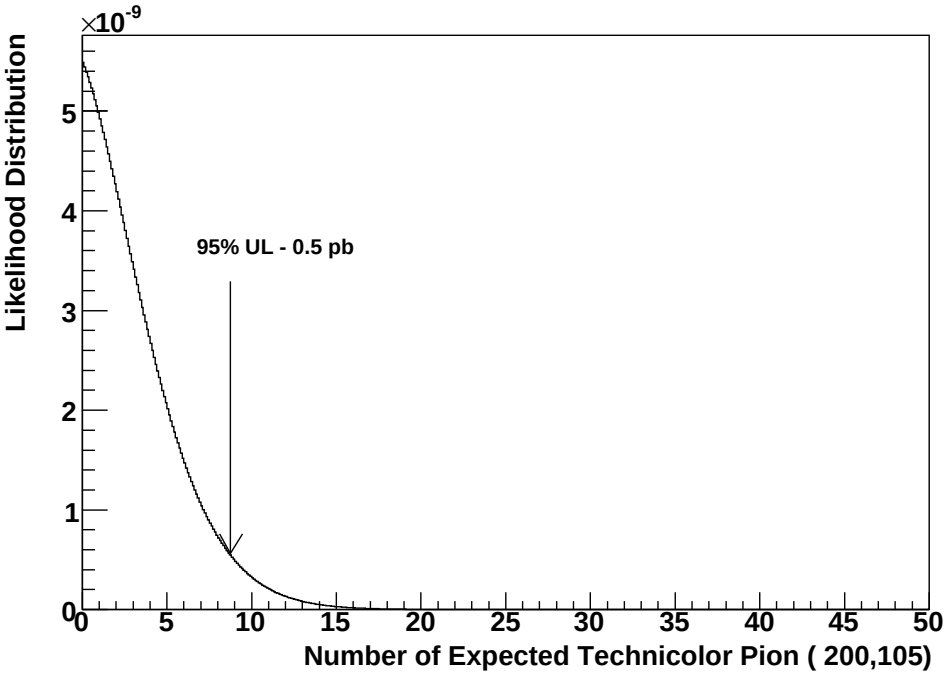

FIG. 16: Likelihood distribution for 95% C.L. upper limit (top) and 95% expected C.L. upper limit (bottom) for techniparticle $\rho_T \rightarrow W\pi_T$ ($M(\rho_T) = 200$ GeV, $M(\pi_T) = 105$ GeV and $M_V = 500$ GeV).

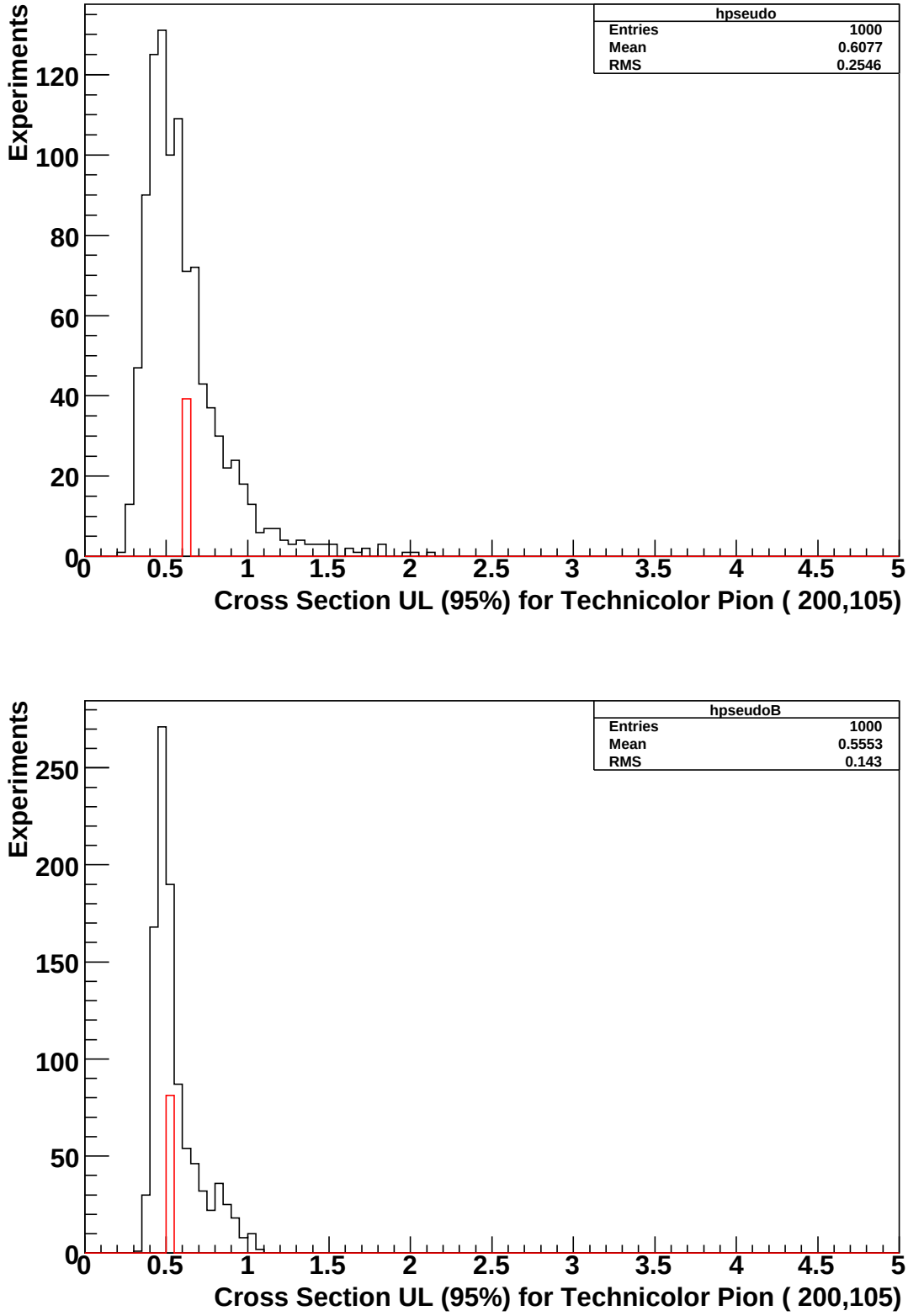

FIG. 17: Pseudo-experiment results using the uncertainties in signal and background for observed 95% C.L. upper limit (top) and expected 95% C.L. upper limit (bottom) on the production cross section for techniparticle $W\pi_T$ for $M(\rho_T) = 200$ GeV, $M(\pi_T) = 105$ GeV and $M_V = 500$ GeV. Red histograms indicate the mean of these distribution (top plot) and in the bottom plot gives the final 95% observed C.L. upper limit on the cross section in our data.

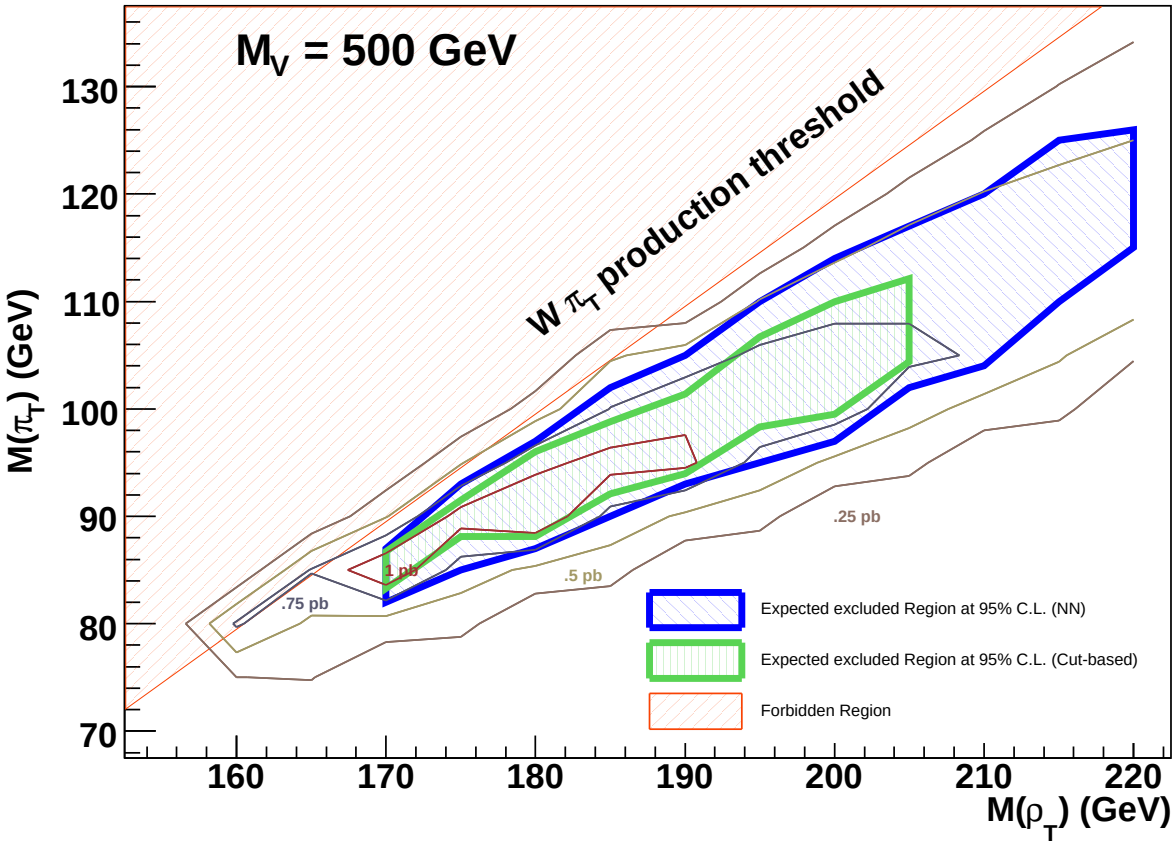

FIG. 18: Expected excluded region at 95% C.L. in the $(M(\rho_T), M(\pi_T))$ plane for $\rho_T \to W\pi_T \to e\nu\ b\bar{b}(\bar{c})$ production with $M_V = 500$ GeV calculated using 388 pb $^{-1}$ of DØ data for topological analysis (green shaded area) and neural network (blue shaded area). The red shaded area define where $W\pi_T$ production is kinematically forbidden. The four iso-cross section curves indicates areas in the $(M(\rho_T), M(\pi_T))$ plane where cross section times branching ratio is ≥ 1 pb (red curve), ≥ 0.75 pb (blue curve), ≥ 0.5 pb (mustard curve) and ≥ 0.25 pb (brown curve).

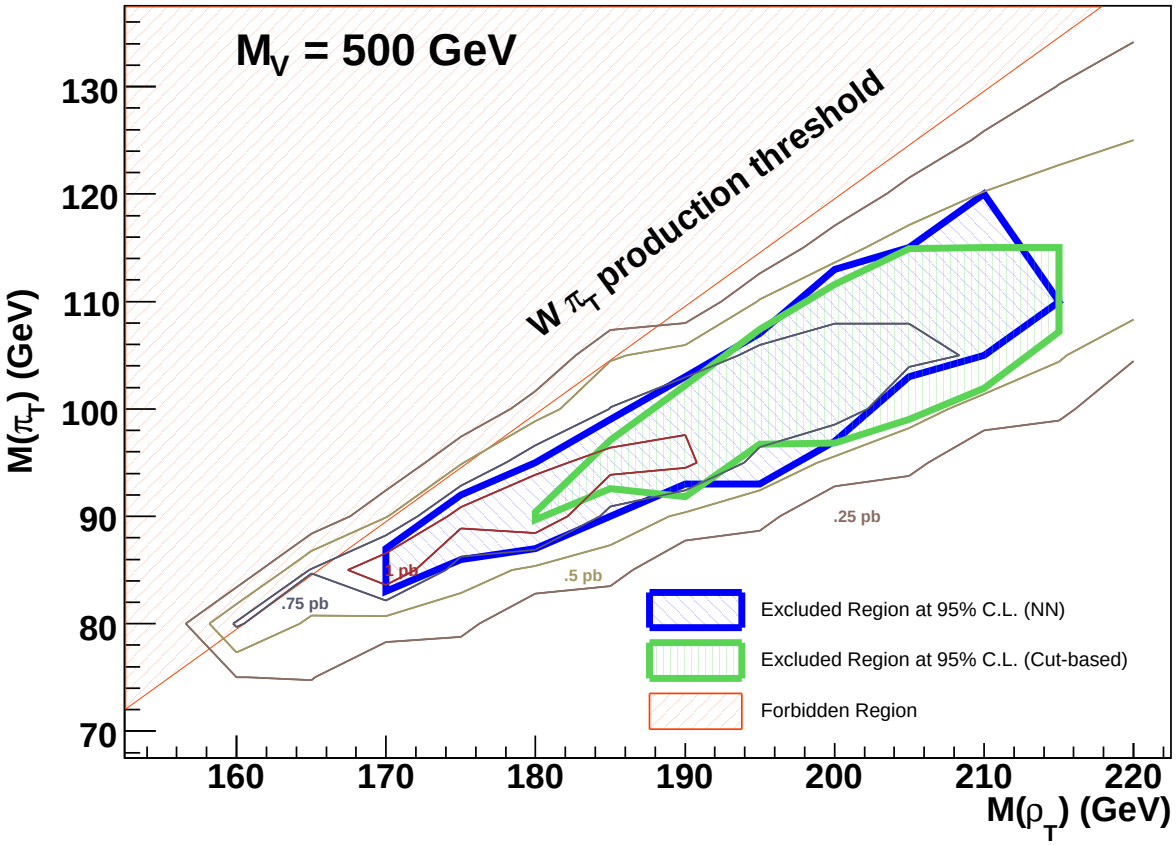

FIG. 19: Excluded region at 95% C.L. in the $(M(\rho_T), M(\pi_T))$ plane for $\rho_T \to W\pi_T \to e\nu\, b\bar{b}(\bar{c})$ production with $M_V = 500$ GeV calculated using 388 pb $^{-1}$ of DØ data with the cut-based analysis (green contour) and with the neural network analysis (blue contour). The red line define the kinematic threshold for $W\pi_T$ production. The four iso-cross section curves indicates areas in the M_{ρ_T}, M_{π_T} plane where the expected cross section times branching ratio is ≥ 1 pb (red curve), ≥ 0.75 pb (blue curve), ≥ 0.5 pb (mustard curve) and ≥ 0.25 pb (brown curve).

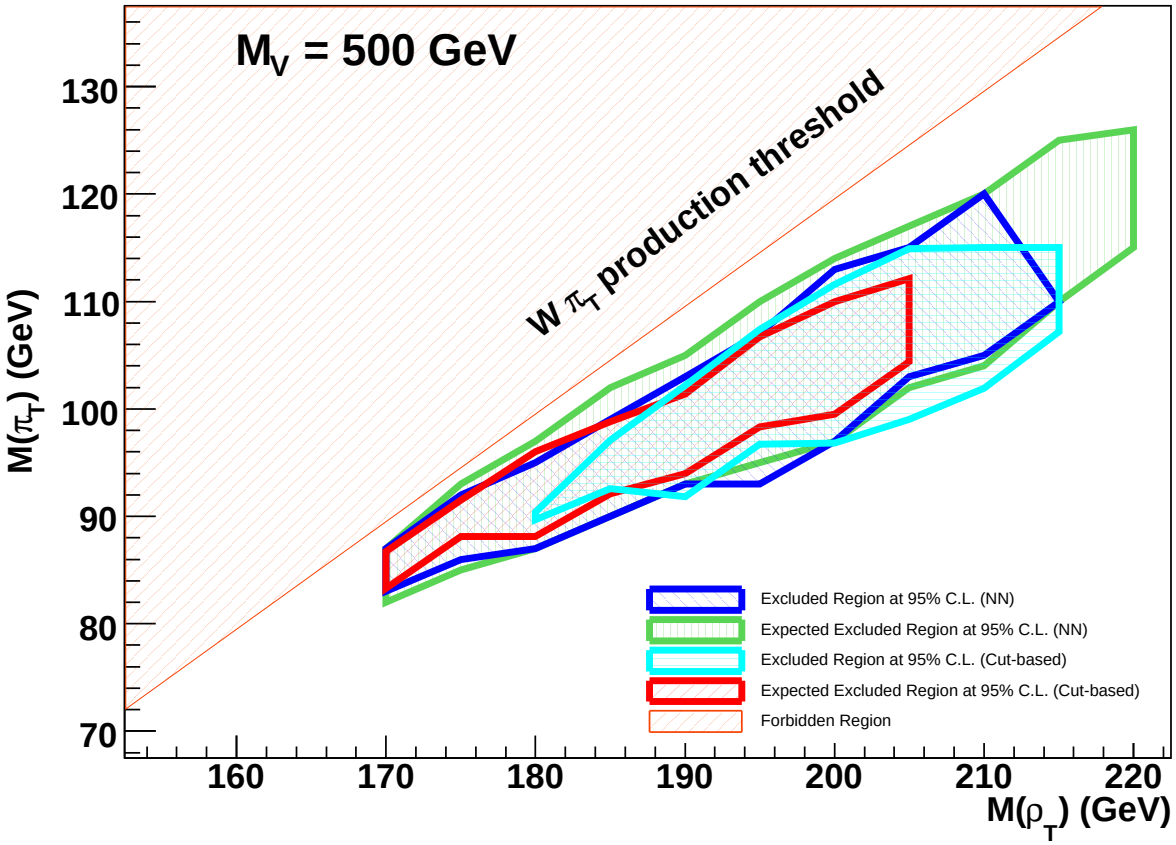

FIG. 20: Expected and observed excluded region at 95% C.L. in the $(M(\rho_T), M(\pi_T))$ plane for $\rho_T \to W\pi_T \to e\nu\ b\bar{b}(\bar{c})$ production with $M_V = 500$ GeV calculated using 388 pb $^{-1}$ of DØ data for cut-based analysis and neural network analysis. The red shaded area define where $W\pi_T$ production is kinematically forbidden.